Neutrinos from STORed Muons
Letter of Intent

P. Kyberd
Brunel University

C. Ankenbrandt, S. J. Brice, A. D. Bross, J. Kopp, N. Mokhov, M. Popovic, and S. Striganov
Fermi National Accelerator Laboratory

A. Blondel and A. Bravar
University of Geneva

R. Bayes and P. Soler
University of Glasgow

A. Dobbs, K. Long, J. Pasternak, and M. O. Wascko
Imperial College London

S. K. Agarwalla
Instituto de Fisica Corpuscular, CSIC and Universidad de Valencia

S. A. Bogacz
Jefferson Laboratory

Y. Mori
Kyoto University

A. de Gouvêa
Northwestern University and
Osaka University

Y. Kuno and A. Sato
Osaka University

J. Cobb and C. D. Tunnell
Oxford University, Subdepartment of Particle Physics

W. Winter
Institut für theoretische Physik und Astrophysik, Universität Würzburg

(Dated: April 30, 2012)

CONTENTS

I. OVERVIEW

The idea of using a muon storage ring to produce a high-energy ($\simeq$ 50 GeV) neutrino beam for experiments was first discussed by Koshkarev [1]. However, a detailed description of the concept for neutrino oscillation experiments was first produced by Neuffer [2] in 1980. The facility we describe here (νSTORM) is essentially the same facility proposed in 1980 and would utilize a 3-4 GeV/c muon storage ring to study eV-scale oscillation physics and, in addition, could add significantly to our understanding of ν_e and ν_μ cross sections. In particular the facility can:

1. Address the large Δm^2 oscillation regime and make a major contribution to the study of sterile neutrinos.
2. Make precision ν_e and $\bar{\nu}_e$ cross-section measurements.
3. Provide a technology (μ decay ring) test demonstration and μ beam diagnostics test bed.
4. Provide a precisely understood ν beam for detector studies

The facility is the simplest implementation of the Neutrino Factory concept [3]. In our case, 60 GeV protons are used to produce pions off a conventional solid target. The pions are collected with a focusing device (horn or Li lens) and are then transported to and injected into a storage ring where they decay to muons. The muons then subsequently decay into electrons and neutrinos. We are starting with a storage ring design that is optimized for 3.8 GeV/c muon momentum. In this case, the energy is optimized for the needs of both the oscillation and the cross section physics. See Fig. 1 for a schematic of the facility.

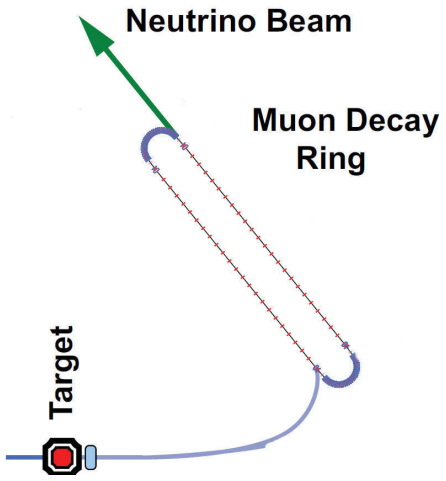

Figure 1. Schematic of the facility

For positive muons, the decay, $\mu^+ \rightarrow e^+ + \bar{\nu}_\mu + \nu_e$, yields a neutrino beam of precisely known flavor content and energy. In addition, if the circulating muon flux in the ring is

measured accurately (with beam-current transformers, for example) then the neutrino beam flavor content and flux are precisely known. Near and far detectors are placed along one of the straight sections of the racetrack decay ring. The near detector can be placed at 20-50 meters from the end of the straight and will measure neutrino-nucleon cross sections that are potentially important for future long-baseline experiments. This would include the first precision measurements of ν_e and $\bar{\nu}_e$ cross sections. A far detector at 800-1000 m would study neutrino oscillation physics and would be capable of performing searches in both appearance and disappearance channels. The experiment will take advantage of the "golden channel" of oscillation appearance $\nu_e \rightarrow \nu_\mu$, where the resulting final state has a muon of the wrong-sign from interactions of the ν_μ in the beam. In the case of μ^+s stored in the ring, this would mean the observation of an event with a μ^-. This detector would need to be magnetized for the wrong-sign muon appearance channel, as is the case for the current baseline Neutrino Factory detector [4]. A number of possibilities for the far detector exist. However, a magnetized iron detector similar to that used in MINOS is likely to be the most straightforward approach for the far detector design. For the purposes of the νSTORM oscillation physics, a detector inspired by MINOS, but with thinner plates and much larger excitation current (larger B field) is assumed.

II. THEORETICAL AND EXPERIMENTAL MOTIVATION

A. Sterile neutrinos in extensions of the Standard Model

Sterile neutrinos—fermions that are uncharged under the $SU(3) \times SU(2) \times U(1)$ gauge group—arise naturally in many extensions of the Standard Model and even where they are not an integral part of a model, they can usually be accomodates easily. A detailed overview of the phenomenology of sterile neutrino and of related model building considerations is given in [5].

For instance, in Grand Unified Theories (GUTs), fermions are grouped into multiplets of a large gauge group, of which $SU(3) \times SU(2) \times U(1)$ is a subgroup. If these multiplets contain not only the known quarks and leptons, but also additional fermions, these new fermions will, after the breaking of the GUT symmetry, often behave like gauge singlets (see for instance [6–9] for GUT models with sterile neutrinos).

Models attempting to explain the smallness of neutrino masses through a seesaw mechanism generically contain sterile neutrinos. While in the most generic seesaw scenarios, these sterile neutrinos are extremely heavy ($\sim 10^{14}$ GeV) and have very small mixing angles ($\sim 10^{-12}$) with the active neutrinos, slightly non-minimal seesaw models can easily feature sterile neutrinos with eV-scale masses and with per cent level mixing with the active neutrinos. Examples for non-minimal seesaw models with relatively light sterile neutrinos include the split seesaw scenario [10], seesaw models with additional flavor symmetries (see e.g. [11]), models with a Froggatt-Nielsen mechanism [12, 13], and extended seesaw models that augment the mechanism by introducing more than three singlet fermions, as well as additional symmetries [14–16].

Finally, sterile neutrinos arise naturally in "mirror models", in which the existence of an extended "dark sector", with nontrivial dynamics of its own, is postulated. If the dark sector is similar to the visible sector—as is the case, for instance in string-inspired $E_8 \times E_8$ models—it is natural to assume that it also contains neutrinos [17–19].

B. Experimental hints for light sterile neutrinos

While the theoretical motivation for the existence of sterile neutrinos is certainly strong, what has mostly prompted the interest of the scientific community in this topic is is the fact that there are several experimental results that show significant deviations from the Standard Model predictions which can be interpreted as hints for oscillations involving sterile neutrinos.

The first of these hints was obtained by the **LSND** collaboration, who carried out a search for $\bar{\nu}_\mu \to \bar{\nu}_e$ oscillations over a baseline of ~ 30 m [20]. Neutrinos were produced

in a stopped pion source in the decay $\pi^+ \to \mu^+ + \nu_\mu$ of pions at rest and the subsequent decay $\mu^+ \to e^+ \bar{\nu}_\mu \nu_e$. Electro antineutrinos are detected through the inverse beta decay reaction $\bar{\nu}_e p \to e^+ n$ in a liquid scintillator detector. Backgrounds to this search arise from the decay chain $\pi^- \to \bar{\nu}_\mu + (\mu^- \to \nu_\mu \bar{\nu}_e e^-)$ if negative pions produced in the target decay before they are captured by a nucleus, and from the reaction $\bar{\nu}_\mu p \to \mu^+ n$, which is only allowed for the small fraction of muon antineutrinos produced by pion decay *in flight* rather than stopped pion decay. The LSND collaboration finds an excess of $\bar{\nu}_e$ candidate events above this background with a significance of more than 3σ. When interpreted as $\bar{\nu}_\mu \to \bar{\nu}_e$ oscillations through an intermediate sterile state $\bar{\nu}_s$, this result is best explained by sterile neutrinos with an effective mass squared splitting $\Delta m^2 \gtrsim 0.1$ eV^2 relative to the active neutrinos, and with an effective sterile-induced $\bar{\nu}_\mu$–$\bar{\nu}_e$ mixing angle $\sin^2 2\theta_{e\mu,\text{eff}} \gtrsim 2 \times 10^{-3}$, depending on Δm^2.

The **MiniBooNE experiment** [21, 22] was designed to test the neutrino oscillation interpretation of the LSND result using a different technique, namely neutrinos from a horn-focused pion beam. While a MiniBooNE search for $\nu_\mu \to \nu_e$ oscillations indeed disfavors most (but not all) of the parameter region preferred by LSND in the simplest model with only one sterile neutrino [21], the experiment obtains results *consistent* with LSND when running in antineutrino mode and searching for $\bar{\nu}_\mu \to \bar{\nu}_e$. Due to low statistics, however, the antineutrino data favors LSND-like oscillations over the null hypothesis only at the 90% confidence level. Moreover, MiniBooNE observes a yet unexplained 3.0σ excess of ν_e-like events (and, with smaller significance also of $\bar{\nu}_e$ events) at low energies, 200 MeV $\lesssim E_\nu \lesssim$ 475 MeV, outside the energy range where LSND-like oscillations would be expected.

A third hint for the possible existence of sterile neutrinos is provided by the so-called **reactor antineutrino anomaly**. In 2011, Mueller et al. published a new ab initio computation of the expected neutrino fluxes from nuclear reactors [23]. Their results improve upon a 1985 calculation by Schreckenbach [24] by using up-to-date nuclear databases, a careful treatment of systematic uncertainties and various other corrections and improvements that were neglected in the earlier calculation. Mueller et al. find that the predicted antineutrino flux from a nuclear reactor is about 3% higher than previously thought. This result, which was later confirmed by Huber [25], implies that short baseline reactor experiments have observed a 3σ *deficit* of antineutrinos compared to the prediction [26].[5] It needs to be emphasized that the significance of the deficit depends crucially on the systematic uncertainties associated with the theoretical prediction, some of which are difficult to estimate reliably. If the reactor antineutrino deficit is interpreted as $\bar{\nu}_e \to \bar{\nu}_s$ disappearance via oscillation, the required 2-flavor oscillation parameters are $\Delta m^2 \gtrsim 1$ eV^2 and $\sin^2 2\theta_{ee,\text{eff}} \sim 0.1$.

Such short-baseline oscillations could also explain another experimental result: The **Gallium anomaly**. The GALLEX and SAGE solar neutrino experiments used electron neutrinos from intense artifical radioactive sources to test their radiochemical detection principle [27–31]. Both experiments observed fewer ν_e from the source than expected. The statistical significance of the deficit is above 99% and can be interpreted in terms of short-baseline $\bar{\nu}_e \to \bar{\nu}_s$ disappearance with $\Delta m^2 \gtrsim 1$ eV^2 and $\sin^2 2\theta_{ee,\text{eff}} \sim 0.1$–$0.8$. [32–34].

C. Constraints and global fit

While the previous section shows that there is an intriguing accumulation of hints for the existence of new oscillations effects—possibly related to sterile neutrinos—in short-baseline experiments, these hints are not undisputed. Several short-baseline oscillation experiments did *not* confirm the observations from LSND, MiniBooNE, reactor experiments, and Gallium experiments, and place very strong limits on the relevant regions of parameter space in sterile neutrino models. To assess the viability of these models it is necessary to carry out a global fit to all relevant experimental data sets, and several groups have endeavored to do so [35–39] [5]. In figure 2 [35] [5], we show the current constraints on the parameter space of a $3+1$ model (a model with three active neutrinos and one sterile neutrino). We have projected the parameter space onto a plane spanned by the mass squared difference Δm^2 between the heavy, mostly sterile mass eigenstate and the light, most active ones and by the effective amplitude $\sin^2 2\theta_{e\mu,\text{eff}}$ for $\nu_\mu \to \nu_e$ 2-flavor oscillations to which LSND and MiniBooNE are sensitive.

We see that there is severe tension in the global data set: The parameter region favored by LSND and MiniBooNE antineutrino data is disfavored at more than 99% confidence level by searches for $\langle\bar{\nu}\rangle_e$ and $\langle\bar{\nu}\rangle_\mu$ disappearance. Using a parameter goodness of fit test [59] to quantity this tension, p-values on the order of few $\times 10^{-6}$ are found for the comparibility of LSND and MiniBooNe $\bar{\nu}$ data with the rest of the global data set, and p-values smaller than 10^{-3} are found for the compatibility of appearance data and disappearance data [5]. The global fit improves somewhat in models with more than one sterile neutrino, but significant tension remains [35] [5].

One can imagine several possible resolutions to this puzzle:

1. One or several of the apparent deviations from the standard three neutrino oscillation framework discussed in section II B have explanations not related to sterile neutrinos.

2. One or several of the null results that favor the no-oscillation hypothesis are in error.

3. There are more than two sterile neutrino flavors. Note that already scenarios with one sterile neutrino with an eV scale mass are in some tension with cosmology, even though the existence of one sterile neutrino with a mass well below 1 eV is actually preferred by cosmological fits [60–63]. Cosmological bounds on sterile neutrinos can be avoided in non-standard cosmologies [64] or by invoking mechanisms that suppress sterile neutrino production in the early universe [65, 66].

4. There are sterile neutrinos plus some other kind of new physics at the eV scale. (See for instance [58, 67] for an attempt in this direction.)

We conclude that our understanding of short baseline neutrino oscillations is currently in a rather unsatisfactory state. On the one hand, several experiments indicate deviations from the established three-neutrino framework. However, none of these hints can be considered

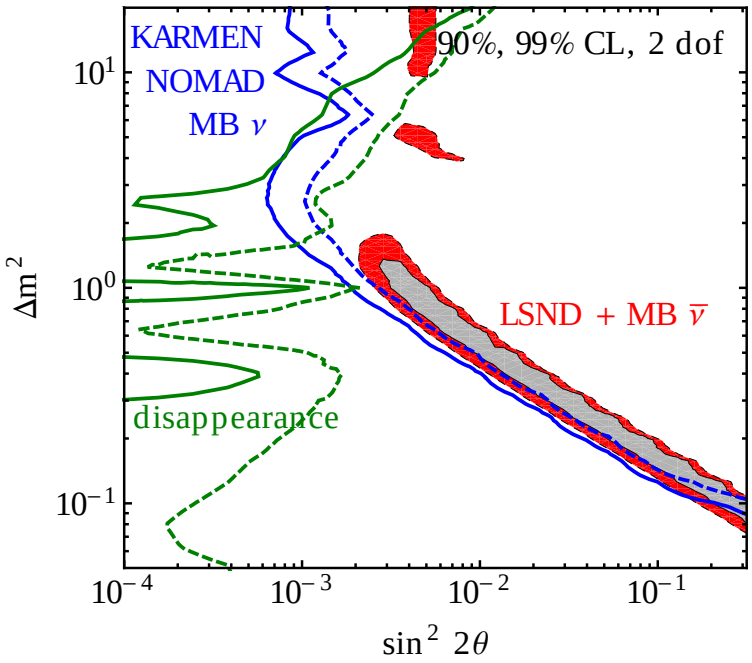

Figure 2. Global constraints on sterile neutrinos in a 3+1 model. We show the allowed regions at 90% and 99% CL from a combined analysis of the LSND [20] and MiniBooNE antineutrino [22] signals (filled regions), as well as the constraints from the null results of KARMEN [40], NOMAD [41] and MiniBooNE neutrino [21] appearance searches (blue contour). The limit from disappearance experiments (green contours) includes data from CDHS [42], atmospheric neutrinos [43], MINOS [44, 45], and from SBL reactor experiments [46–53]. For the latter, we have used the new reactor flux predictions from [23], but we have checked that the results, especially regarding consistency with LSND and MiniBooNE $\bar{\nu}$ data, are qualitatively unchanged when the old reactor fluxes are used. Fits have been carried out in the GLoBES framework [54, 55] using external modules discussed in [56–58].

conclusive, and moreover, when interpreted in the simplest sterile neutrino models, they are in severe tension with existing constraints on the parameter space of these models. An experiment searching for short-baseline neutrino oscillations with good sensitivity and well-controlled systematic uncertainties has great potential to clarify the situation by either finding a new type of neutrino oscillation or by deriving a strong and robust constraint on any such oscillation. While the former outcome would constitute a major discovery, also the latter one would certainly receive a lot of attention since it would provide the world's strongest constraints on a large variety of theoretical models postulating "new physics" in the neutrino sector at the eV scale.

III. FACILITY

The basic concept was presented in Fig. 1. A high-intensity proton source places beam on a target, producing a large spectrum of secondary pions. Forward pions are focused by a collection lens into a transport channel. π decay within the transport produces μ which are injected into the decay ring. μ-decay within the straight sections will produce ν beams of known flux and flavor via: $\mu^+ \rightarrow e^+ + \bar{\nu}_\mu + \nu_e$ or $\mu^- \rightarrow e^- + \nu_\mu + \bar{\nu}_e$. For a specific implementation, we choose a X GeV/c storage ring to obtain the desired spectrum of X-Y GeV ν. This means that we must capture π at a higher momentum (Z GeV/c).

A. Targeting and capture

Yes we must produce pions.

1. Targeting

B. Injection Options

This scenario requires storage of μ from π decay. The π decay can occur either before injection or in the ring. Decay before injection requires a separate decay transport line and full-aperture fast kickers matching the π beam pulse to the ring. For 3000 GeV/c π, the decay length is 168m; 45With π decay within the Ring, non-Liouvillean stochastic injection is possible. In stochastic injection, the 3 GeV pion beam is transported from the target into the storage ring, dispersion-matched into a long straight section. (Circulating and injection orbits are separated by momentum.) Decays within that straight section provide muons that are within the 2.1 GeV/c ring momentum acceptance. With stochastic injection, μ from a beam pulse as long as the MI circumference (3000m) can be accumulated, and no injection kickers are needed, see Fig. 3

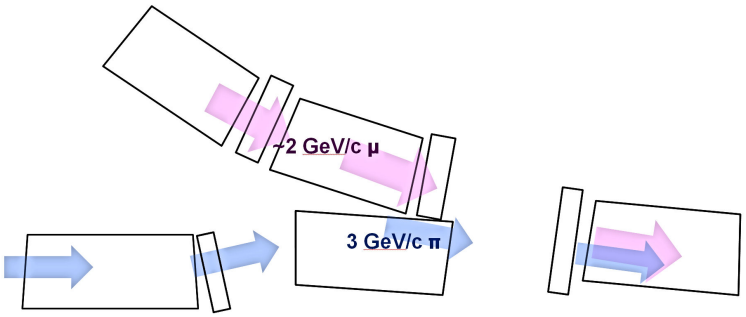

Figure 3. Stocastic injection concept

C. Decay ring

1. FODO

2. Racetrack FFAG

IV. FAR DETECTOR - SUPERBIND

The Super B Iron Neutrino Detector (SuperBIND) is an iron and scintillator sampling calorimeter which is similar in concept to the MINOS near detector [68]. We have chosen a cross section of approximately 5 m in order to maximize the ratio of the fiducial mass to total mass. The magnetic field will be toroidal as in MINOS and SuperBIND will also use extruded scintillator for the readout plans. Details on the iron plates, magnetization, scintillator, photodetector and electronics are given below. Fig. 4 gives a overall schematic of the detector.

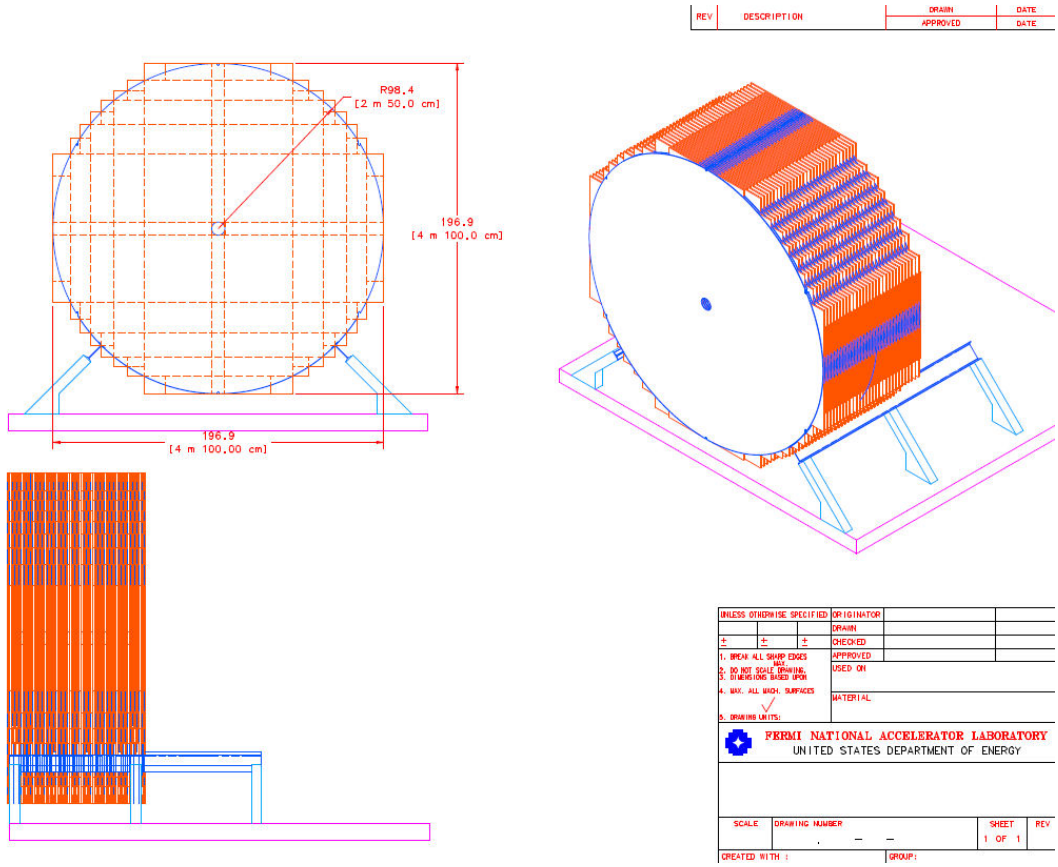

Figure 4. Far Detector concept

A. Iron Plates

For the Iron plates in SuperBIND, we are following the following design strategy. The plates are circles with overall dimension of 5 m and 1.0 cm thick. They are fabricated from two semicircles that are skip welded together. Instead of hanging the plates on ears (as was done in MINOS), we plan to stack in a cradle using a strong-back when starting the stacking. We envision that no R&D on the iron plates will bbe needed. Final specification of the plate structure would be determined once a plate fabricator is chosen.

B. Magnetization

As was mentioned above, MIND will have a toroidal magnetic field like that of MINOS. For excitation, however, we plan to use the concept of the Superconducting Transmission Line (STL)developed for the Design Study for a Staged Very Large Hadron Collider [69]. In order to obtain the highest field possible in the iron plates in order to minimize the muon charge mis-ID rate, SuperBIND requires a much large excitation current-turn than that which is used in the MINOS near detector (40 kA-turns). We have simulated 3 turns of the STL (20 cm hole). The SCT consists of a cylindrical superconducting braid inside a pipe cooled by supercritical helium. The superconductor and cryo-pipe are co-axial to a cyclindrical cryostat/vacuum vessel, Fig. 5. Fig. 5 shows the constructions details for the STL that was prototyped and tested for the VLHC study and consisted of: 1. A perforated Invar flow liner and support, 2. A copper stabilizer braid, 3. Superconductor cable braid, 4. An Invar pipe that contains the helium, 5. The cold-pipe support, 6. Cryoshield, 7. Superinsulation and 8. The vacuum jacket/pipe. Utilizing the SuperBIND plate geometry shown in Fig. 4,

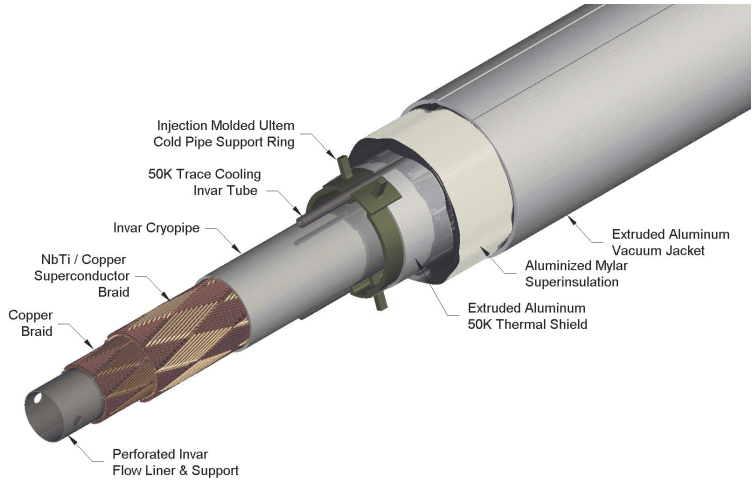

Figure 5. Superconducting transmission line

a 2-d finite element analysis of the plate was done. Fig. 6 shows model (1/8th) that was used in the analysis. A 20 cm diameter hole for the SCT was assumed and the CMS steel {citeSmith:2004uf BH curve was assumed. For this analysis, an excitation current of 250 kA-turn was used. This represents approximately 80% of the critical current acheived at 6.5K in the STL test stand assembled for the VLHC proof-of-principle.

C. Detector planes

1. Scintillator

Particle detection using extruded scintillator and optical fibres is a mature technology. MINOS has shown that co-extruded solid scintillator with embedded wavelength shifting (WLS)

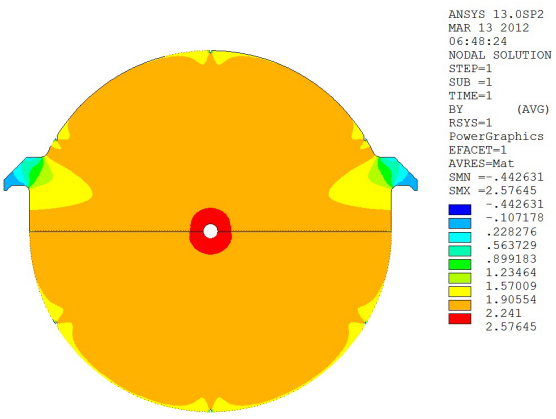

Figure 6. Toroidal Field Map

fibres and PMT readout produces adequate light for MIP tracking and that it can be manufactured with excellent quality control and uniformity in an industrial setting. Many experiments use this same technology for the active elements of their detectors, such as the K2K Scibar [70], the T2K INGRID, the T2K P0D, the T2K ECAL [71] and the Double-Chooz detectors [72].

Our initial concept for the readout planes for SuperBIND is to have both an x and a y view between each plate. The simulations done to date have assumed a scintillator extrusion profile that is 1.0 $\times$ 1.0 cm^2. This gives both the required point resolution and light yield.

2. Rectangular extrusions

The existing SuperBIND simulations have assumed that the readout planes will use a rectangular extrusion that is 1.0 $\times$ 1.0 cm^2. A 1 mm hole down the centre of the extrusion is provided for insertion of the wavelength shifting fibre. This is a relatively simple part to manufacture and has already been fabricated in a similar form for a number of small-scale applications. The scintillator strips will consist of an extruded polystyrene core doped with blue-emitting fluorescent compounds, a co-extruded TiO_2 outer layer for reflectivity, and a hole in the middle for a WLS fibre. Dow Styron 665 W polystyrene pellets are doped with PPO (1% by weight) and POPOP (0.03% by weight). The strips have a white, co-extruded, 0.25 mm thick TiO_2 reflective coating. This layer is introduced in a single step as part of a co-extrusion process. The composition of this capstocking is 15% TiO_2 (rutile) in polystyrene. In addition to its reflectivity properties, the layer facilitates the assembly of the scintillator strips into modules. The ruggedness of this coating enables the direct gluing of the strips to each other and to the module skins which results in labour and time savings for the experiment. This process has now been used in a number of experiments.

D. Photo-detector

Given the rapid development in recent years of solid-state photodetectors based on Geiger mode operation of silicon avalanche photodiodes, we have chosen this technology for MIND. Although various names are used for this technology, we will use silicon photomultiplier or SiPM.

1. SiPM Overview

SiPM is the often-used name for a type of photo detector formed by combining many small avalanche photodiodes operated in the Geiger mode to form a single detector [73, 74]. Detailed information and basic principles of operation of these "multi-pixel" photodiodes can be found in a recent review paper and the references therein [**?**]. The first generation of these detectors use a polysilicon resistor connected to each avalanche photodiode forming a pixel. Pixels usually vary in size from 10 $\times 10\,\mu\mathrm{m}^2$ to 100 $\times 100,\mu\mathrm{m}^2$ (see figure 7). All the diodes are connected to a common electrical point on one side, typically through the substrate, and all the resistors are connected to a common grid with metal traces on the other side to form a two node device. A typical SiPM will have from 100 to 10,000 of these pixels in a single device, with the total area from 1 to 10 mm^2. Because all the diode and the individual quenching resistors are connected in parallel, the SiPM device as a whole appears as a single diode. In operation, the device appears to act somewhat like a conventional APD, but in detail it is radically different. Because the diodes are operated in the Geiger mode, and because every pixel of the SiPM device is nearly identical, the sum of the fired pixels gives the illusion of an analog signal that is proportional to the incident light, but it is an essentially digital device.

SiPMs have a number of advantages over conventional photomultiplier tubes, including very high photon-detection efficiency, complete immunity to magnetic fields, excellent timing characteristics, compact size, and physical robustness. They are particularly well suited to applications with fibres, as the natural size of the SiPM is comparable to that of fibres [75, 76]. But the most important single feature of the SiPM is that it can be manufactured in standard microelectronics facilities using nearly standard CMOS processing. This means that huge numbers of devices can be produced without any manual labour, making the SiPMs very economical. Furthermore, it is possible to integrate the electronics into the SiPM itself, which reduces cost and improves performance. Initial steps have been taken in this direction, though most current SiPMs are not manufactured in this way. But it is widely recognized that this is the approach that makes sense in the long run for most applications. It improves performance and reduces cost, and can be tailored to a specific application. As the use of SiPMs spreads, so will the use of custom SiPMs with integrated electronics, just as ASICs have superseded standard logic in electronics. The photon detection efficiency (PDE) of a SiPM is the product of 3 factors:

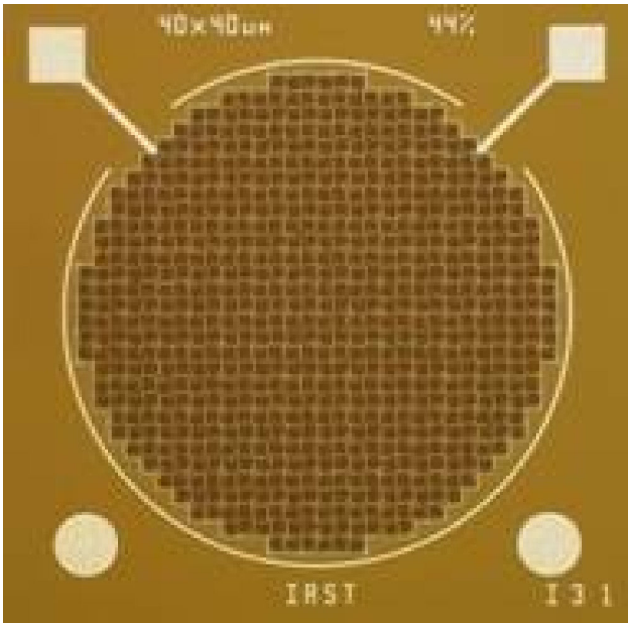

Figure 7. Photograph of SiPM

$$\text{PDE} = QE \cdot \varepsilon_{Geiger} \cdot \varepsilon_{pixel}, \tag{1}$$

where QE is the wavelength-dependent quantum efficiency, ε_{Geiger} is the probability to initiate the Geiger discharge by a photoelectron, and ε_{pixel} is the fraction of the total photodiode area occupied by sensitive pixels. The bias voltage affects one parameter in the expression (1), ε_{Geiger}. The geometrical factor ε_{pixel} is completely determined by the photodiode topology, and is in the range 50-70%. The PDE of a device manufactured by Hamamatsu (Hamamatsu uses the name multi-pixel photon counter, MPPC) as function of wavelength of detected light is shown in figure 8.

2. Readout Electronics

On the periphery of the chip there is circuitry that latches the number of fired pixels in a FIFO, adds a time stamp and issues periodic latch resets to the quenching circuits. The communication with the chip is serial, with an input, an output and a clock, all of which are differential signals. SiPM bias and ground complete the connections for a total of eight. The power for the digital circuitry on the chip is extracted from the clock lines. A number of chips would be connected with flex cables, in a ring topology, to a data concentrator module which would service a large number of SiPMs. A reasonable bandwidth available on differential lines over a flex cable for distances up to a few meters is between 10 Mbps and 100 Mbps. Depending on the rate of signals in the detector, and including things such as protocol overhead and data redundancy, a reasonable estimate of the number of SiPM chips that can be serviced by a single data concentrator is a few thousand. We expect that in this

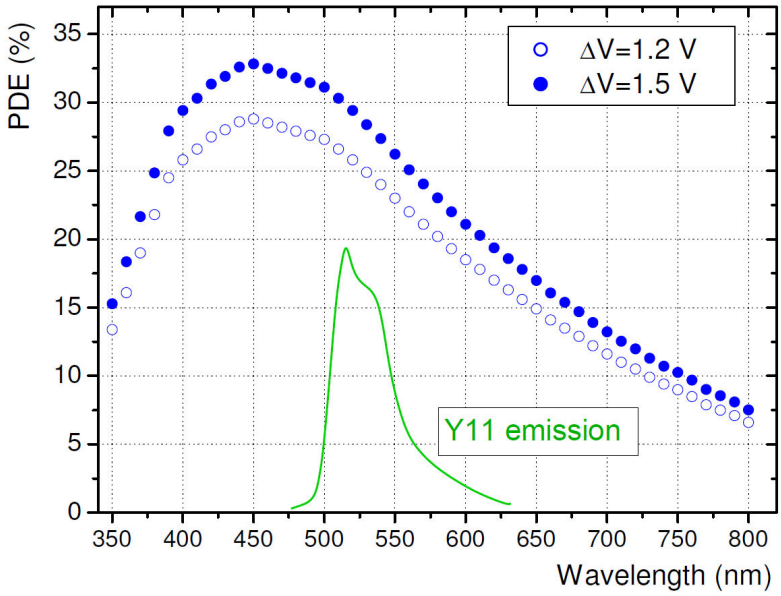

Figure 8. Photon detection efficiency of a Hamamatsu MPPC as a function of wavelength of the detected light at ΔV of 1.2 and 1.5 V at 25°C. The Y11(150 ppm) Kuraray fibre emission spectrum (in a. u.) for fibre length of 150 cm (from Kuraray specification) is also shown.

application, the number of SiPMs in a module associated with a single data concentrator would be limited by mechanical and operational considerations to something like 250 to 500. From the data concentrator, the data travel over optical links to higher-level data collectors.

V. NEAR DETECTOR

A. For oscillation physics

B. For cross-section measurements

VI. PERFORMANCE

A. Event rates

The number of muon decays (N_μ) for νSTORM can be defined in terms of the following:

$$N_\mu = (\text{POT}) \times (\pi \text{ per POT}) \times \epsilon_{\text{collection}} \times \epsilon_{\text{transport}} \times \epsilon_{\text{injection}} \times (\mu \text{ per } \pi) \times A_{\text{dynamic}} \times \Omega \quad (2)$$

where (POT) is the number of protons on target, $\epsilon_{\text{collection}}$ is the collection efficiency, $\epsilon_{\text{transport}}$ is the transport efficiency, $\epsilon_{\text{injection}}$ is the injection efficiency, (μ per π) is the chance that an injected pion results in a muon within the acceptance, A_{dynamic} is probability that a muon within the aperture is within the dynamic aperture, and Ω is the fraction of the ring circumference that directs muons at the far detector.

νSTORM assumes 10^{21} POT for a 4-5 year run using 60 GeV protons. The of pions produced per proton on target as a function of energy has been simulated with Mars [77] into a forward cone of 120 mrad. The results of this analysis can be seen in Fig. 9.

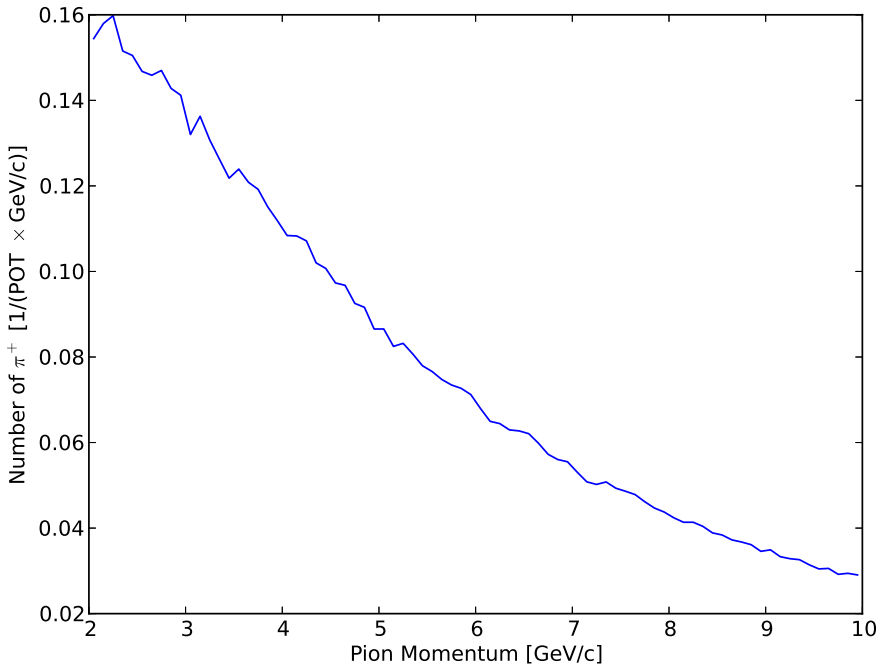

Figure 9. Proton 60 GeV, 70 cm Be target, 1 cm radius, theta less than 120 mrad

Our intial conept for the capture and transport channel is to collect pions within a momentum spread of 10%. Using alinear interpolation, we can integrate $\pi(p)$:

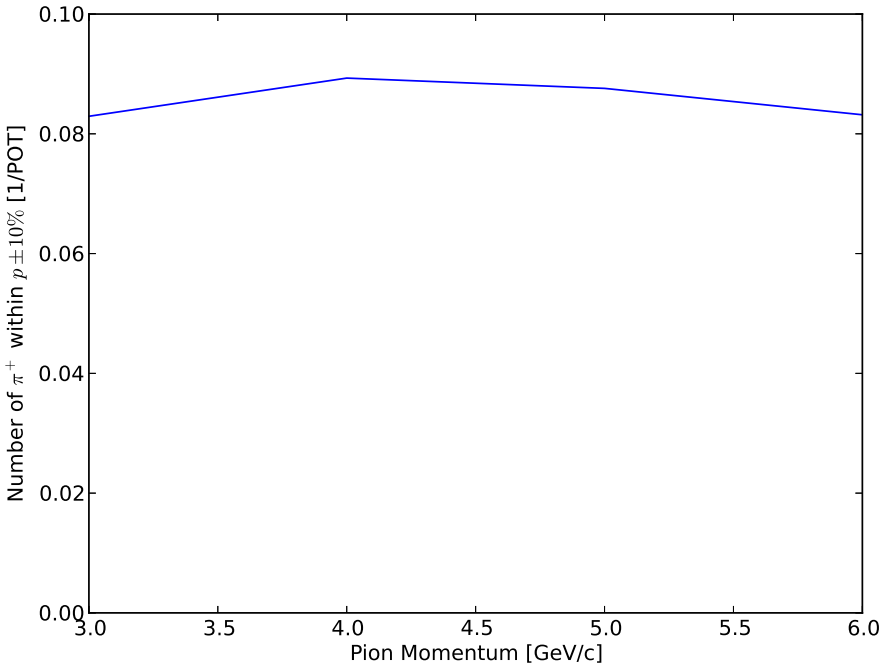

Figure 10. integrated Production

$$(\pi \text{ per POT}) = \int_{p\pm 10\%} \pi(p) \simeq 0.09 \tag{3}$$

where we see that (π per POT) is essentially independent of pion momentum (due to the $\pm 10\%$ momentum acceptance). In Fig. 9 we see that the pion production decreases monotonically with increasing momentum. However, the integration range is relative so the range increases with increasing momentum. These two effects cancel (Fig. 10). We assume a conservative 10% loss of pions during the collection phase, so the efficiency is 90%. The transport efficiency is assumed to be ~ 1. The injection efficiency is assumed to be 90%.

B. Monte Carlo and analysis

C. Sensitivites

1. Appearance channels

2. Disappearance channels

Since disappearance measurements are very sensitive to the signal normalization, additional near detectors have been proposed in $\bar{\nu}_e$ disappearance reactor experiments to measure

θ_{13} [79, 80]. These near detectors are supposed to be as identical as possible as the far detectors, where the main purpose is to control the uncertainty on the reactor neutrino fluxes. This concept has been well established, and can be found in all of the state-of-the-art reactor experiments, such as Double Chooz, Daya Bay, and RENO. For νSTORM, the situation is very similar: while the flux is well under control, cross sections $\times$ efficiencies can be measured by a near detector. However, since oscillations may already take place in the near detector, the oscillation parameters need to be extracted in a self-consistent way in a combined near-far fit [81]. In fact, the near and far detectors may even swap the roles: while for $\Delta m^2 \simeq 1\,\mathrm{eV}^2$, the near detector effectively measures the cross sections and the far detector the oscillation, for $\Delta m^2 \gg 10\,\mathrm{eV}^2$, the near detector measures the oscillations and the far detector (where the oscillations average out) the cross sections.

For the near-far detector combination, there are two crucial issues: the systematics implementation and the treatment of geometry effects. In order to account for the uncertain cross sections $\times$ efficiencies, one can introduce a large systematical error, which is however fully correlated between the two detectors which measure the same flavors and polarities in the disappearance channels. We adopt the most conservative case for this systematics: we even assume a completely unknown shape, i.e., we assume that the cross sections $\times$ efficiencies are unknown to the level of 10% within each bin, uncorrelated among the bins, but fully cor-

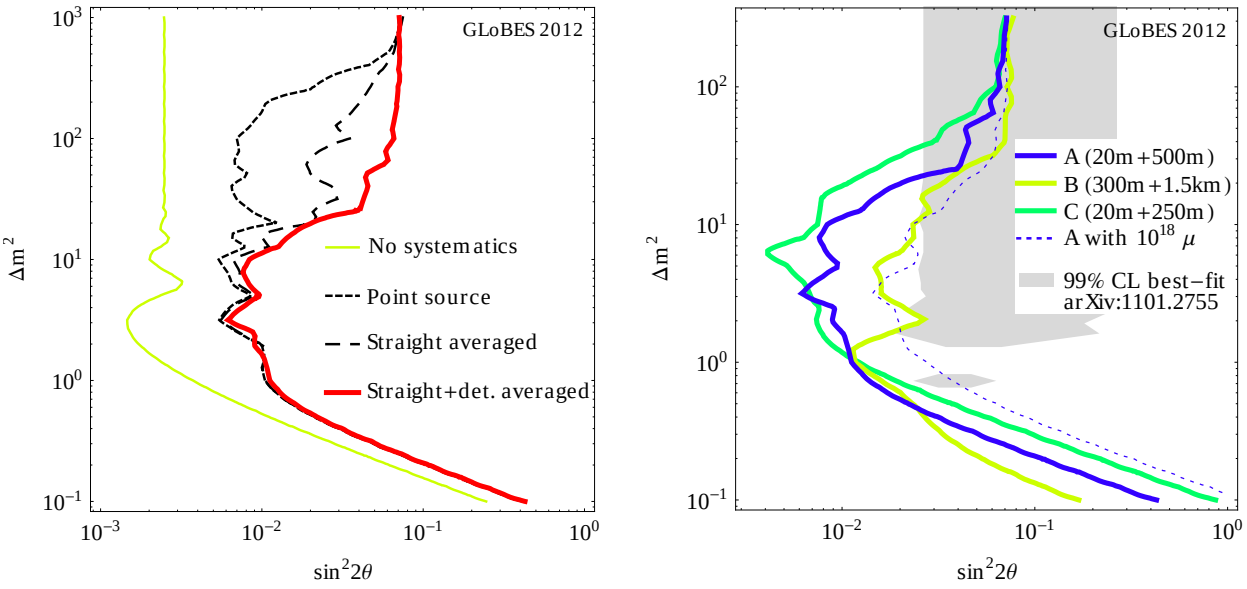

Figure 11. Exclusion region in $\sin^2 2\theta$-Δm^2 (right hand sides of curves) for ν_e disappearance for different geometry assumptions (left panel) and optimization points (right panel); 90% CL, 2 d.o.f. Left panel: The curve "no systematics" represents a single detector at $d = 500\,\mathrm{m}$ using statistics only, whereas the other curves correspond to near-far detector setups, where the red thick curves include (conservative) full systematics, including a 10% shape error, and geometry effects. Right panel: Systematics are fully included, different two-distance optimization points shown (distances to the end of the decay straight). Both panels: $E_\mu = 2\,\mathrm{GeV}$, 10^{19} useful muon decays per polarity, $d_1 = 20\,\mathrm{m}$ (200 t) and $d_2 = 500\,\mathrm{m}$ (1 kt), unless noted otherwise. Figure taken from Ref. [78].

related between the near and far detectors (shape error); for details and further considered systematics see Ref. [78]. Especially for the near detector, geometry effects turn out to be important: the oscillations will average over the finite decay straight [78, 81], and the beam divergence, which cannot be avoided at least from the muon decay kinematics, will lead to a different beam spectrum in the near and far detectors [78, 82]. These effects are illustrated in Fig. 11, left panel, in the two flavor picture: The curve "Point source" shows the sensitivity assuming a point neutrino source and a near detector in the far distance limit, including full systematics. In this curve, a double peak in terms of Δm^2 can be clearly seen, coming from the oscillations taking place in the near ($\Delta m^2 \gg 10\,\mathrm{eV}^2$) or far ($\Delta m^2 \simeq 1\,\mathrm{eV}^2$) detector. If, however, the averaging over the decay straight ("Straight averaged") and the detector geometry ("Straight+detector averaged") are taken into account, the large ($\Delta m^2 \gg 10\,\mathrm{eV}^2$) sensitivity vanishes. The $\sin^2 2\theta$ reach for very large Δm^2 relies on the external knowledge of systematics, in this case it is limited by the 10% shape error.

As far as the two-baseline optimization is concerned [78], the optimal choice depends somewhat on the value of Δm^2. This is illustrated in the right panel of Fig. 11, where the sensitivities for several optimization points are shown. While all of these options perform equally well for $\Delta m^2 \simeq 1\,\mathrm{eV}^2$, larger values of $\Delta m^2 \simeq 1\,\mathrm{eV}^2$ prefer shorter distances (from the end of the decay straight) for the far detector. The optimization point A (20 m+500 m) seems to be a good compromise between the small and large Δm^2 sensitivities for $E_\mu = 2\,\mathrm{GeV}$. This is consistent with the optimization for appearance, but somewhat on the lower end of the optimal baseline range for that. For larger E_μ, slightly longer far detector distances are preferred, which means that 500 m to 800 m seems a reasonable distance range. For the near detector, we find that, in spite of the geometry effects, as short as possible distances are preferred if the far detector is in that baseline range .

As for the absolute performance, we show in Fig. 11 (right panel) the 99% CL best-fit from one of the global (anomaly) fits in the literature for comparison. It is clear that νSTORM can exlcude this region for all of the optimization points for $\Delta m^2 \lesssim 10\,\mathrm{eV}^2$. However, note that either significantly more than 10^{18} useful muon decays per polarity (dashed curve) are needed for that purpose, or muon energies slightly higher than 2 GeV. It can be shown that the proposed setup then has excellent sensitivity to both ν_e and ν_μ disappearance, both for neutrinos and antineutrinos [78], where the details somewhat depend on the final exposure, detection efficiency, and systematics treatment.

D. Cross-sections

VII. OUTLOOK AND CONCLUSIONS

[1] D. G. Koshkarev, "Proposal for a Decay Ring to Produce Intense Secondary Particle Beams at the SPS," (1974), CERN/ISR-DI/74-62.

[2] D. Neuffer, "Design Considerations for a Muon Storage Ring," (1980), Telmark Conference on Neutrino Mass, Barger and Cline eds., Telmark, Wisconsin.

[3] S. Geer, Phys.Rev. **D57**, 6989 (1998), arXiv:hep-ph/9712290 [hep-ph].

[4] S. Choubey *et al.* (The IDS-NF collaboration), (2011), arXiv:1112.2853 [hep-ex].

[5] K. Abazajian, M. Acero, S. Agarwalla, A. Aguilar-Arevalo, C. Albright, *et al.*, (2012), arXiv:1204.5379 [hep-ph].

[6] M. Bando and K. Yoshioka, Prog.Theor.Phys. **100**, 1239 (1998), arXiv:hep-ph/9806400 [hep-ph].

[7] E. Ma, Phys.Lett. **B380**, 286 (1996), arXiv:hep-ph/9507348 [hep-ph].

[8] Q. Shafi and Z. Tavartkiladze, Phys.Lett. **B451**, 129 (1999), arXiv:hep-ph/9901243 [hep-ph].

[9] K. Babu and G. Seidl, Phys.Rev. **D70**, 113014 (2004), arXiv:hep-ph/0405197 [hep-ph].

[10] A. Kusenko, F. Takahashi, and T. T. Yanagida, Phys.Lett. **B693**, 144 (2010), arXiv:1006.1731 [hep-ph].

[11] R. Mohapatra, Phys.Rev. **D64**, 091301 (2001), arXiv:hep-ph/0107264 [hep-ph].

[12] C. Froggatt and H. B. Nielsen, Nucl.Phys. **B147**, 277 (1979).

[13] J. Barry, W. Rodejohann, and H. Zhang, JCAP **1201**, 052 (2012), arXiv:1110.6382 [hep-ph].

[14] R. Mohapatra, S. Nasri, and H.-B. Yu, Phys.Rev. **D72**, 033007 (2005), arXiv:hep-ph/0505021 [hep-ph].

[15] C. S. Fong, R. N. Mohapatra, and I. Sung, Phys.Lett. **B704**, 171 (2011), arXiv:1107.4086 [hep-ph].

[16] H. Zhang, (2011), arXiv:1110.6838 [hep-ph].

[17] Z. G. Berezhiani and R. N. Mohapatra, Phys.Rev. **D52**, 6607 (1995), arXiv:hep-ph/9505385 [hep-ph].

[18] R. Foot and R. Volkas, Phys.Rev. **D52**, 6595 (1995), arXiv:hep-ph/9505359 [hep-ph].

[19] V. Berezinsky, M. Narayan, and F. Vissani, Nucl.Phys. **B658**, 254 (2003), arXiv:hep-ph/0210204 [hep-ph].

[20] A. Aguilar *et al.* (LSND), Phys. Rev. **D64**, 112007 (2001), hep-ex/0104049.

[21] A. Aguilar-Arevalo *et al.* (The MiniBooNE Collaboration), Phys.Rev.Lett. **98**, 231801 (2007), arXiv:0704.1500 [hep-ex].

[22] A. Aguilar-Arevalo *et al.* (The MiniBooNE Collaboration), Phys.Rev.Lett. **105**, 181801 (2010), arXiv:1007.1150 [hep-ex].

[23] T. Mueller, D. Lhuillier, M. Fallot, A. Letourneau, S. Cormon, *et al.*, Phys.Rev. **C83**, 054615 (2011), arXiv:1101.2663 [hep-ex].

[24] K. Schreckenbach, G. Colvin, W. Gelletly, and F. Von Feilitzsch, Phys.Lett. **B160**, 325 (1985).

[25] P. Huber, Phys.Rev. **C84**, 024617 (2011), arXiv:1106.0687 [hep-ph].
[26] G. Mention, M. Fechner, T. Lasserre, T. Mueller, D. Lhuillier, *et al.*, Phys.Rev. **D83**, 073006 (2011), arXiv:1101.2755 [hep-ex].
[27] P. Anselmann *et al.* (GALLEX Collaboration.), Phys.Lett. **B342**, 440 (1995).
[28] W. Hampel *et al.* (GALLEX Collaboration), Phys.Lett. **B420**, 114 (1998).
[29] D. Abdurashitov, V. Gavrin, S. Girin, V. Gorbachev, T. V. Ibragimova, *et al.*, Phys.Rev.Lett. **77**, 4708 (1996).
[30] J. Abdurashitov *et al.* (SAGE Collaboration), Phys.Rev. **C59**, 2246 (1999), arXiv:hep-ph/9803418 [hep-ph].
[31] J. Abdurashitov, V. Gavrin, S. Girin, V. Gorbachev, P. Gurkina, *et al.*, Phys.Rev. **C73**, 045805 (2006), arXiv:nucl-ex/0512041 [nucl-ex].
[32] M. A. Acero, C. Giunti, and M. Laveder, Phys.Rev. **D78**, 073009 (2008), arXiv:0711.4222 [hep-ph].
[33] C. Giunti and M. Laveder, Phys.Rev. **D82**, 053005 (2010), arXiv:1005.4599 [hep-ph].
[34] C. Giunti and M. Laveder, Phys.Rev. **C83**, 065504 (2011), arXiv:1006.3244 [hep-ph].
[35] J. Kopp, M. Maltoni, and T. Schwetz, Phys.Rev.Lett. **107**, 091801 (2011), arXiv:1103.4570 [hep-ph].
[36] C. Giunti and M. Laveder, Phys.Lett. **B706**, 200 (2011), arXiv:1111.1069 [hep-ph].
[37] G. Karagiorgi, (2011), arXiv:1110.3735 [hep-ph].
[38] C. Giunti and M. Laveder, Phys.Rev. **D84**, 093006 (2011), arXiv:1109.4033 [hep-ph].
[39] C. Giunti and M. Laveder, Phys.Rev. **D84**, 073008 (2011), arXiv:1107.1452 [hep-ph].
[40] B. Armbruster *et al.* (KARMEN), Phys. Rev. **D65**, 112001 (2002), arXiv:hep-ex/0203021.
[41] P. Astier *et al.* (NOMAD), Nucl. Phys. **B611**, 3 (2001), arXiv:hep-ex/0106102.
[42] F. Dydak, G. Feldman, C. Guyot, J. Merlo, H. Meyer, *et al.*, Phys.Lett. **B134**, 281 (1984).
[43] Y. Ashie *et al.* (Super-Kamiokande), Phys. Rev. **D71**, 112005 (2005), hep-ex/0501064.
[44] P. Adamson *et al.* (The MINOS Collaboration), Phys.Rev. **D81**, 052004 (2010), arXiv:1001.0336 [hep-ex].
[45] P. Adamson *et al.* (MINOS Collaboration), Phys.Rev.Lett. (2011), arXiv:1104.3922 [hep-ex].
[46] Y. Declais, J. Favier, A. Metref, H. Pessard, B. Achkar, *et al.*, Nucl.Phys. **B434**, 503 (1995).
[47] Y. Declais, H. de Kerret, B. Lefievre, M. Obolensky, A. Etenko, *et al.*, Phys.Lett. **B338**, 383 (1994).
[48] A. Kuvshinnikov, L. Mikaelyan, S. Nikolaev, M. Skorokhvatov, and A. Etenko, JETP Lett. **54**, 253 (1991).
[49] G. Vidyakin, V. Vyrodov, I. Gurevich, Y. Kozlov, V. Martemyanov, *et al.*, Sov.Phys.JETP **66**, 243 (1987).
[50] H. Kwon, F. Boehm, A. Hahn, H. Henrikson, J. Vuilleumier, *et al.*, Phys.Rev. **D24**, 1097 (1981).
[51] G. Zacek *et al.* (CALTECH-SIN-TUM), Phys. Rev. **D34**, 2621 (1986).
[52] M. Apollonio *et al.* (CHOOZ), Eur. Phys. J. **C27**, 331 (2003), hep-ex/0301017.
[53] F. Boehm, J. Busenitz, B. Cook, G. Gratta, H. Henrikson, *et al.*, Phys.Rev. **D64**, 112001 (2001), arXiv:hep-ex/0107009 [hep-ex].

[54] P. Huber, M. Lindner, and W. Winter, Comput. Phys. Commun. **167**, 195 (2005), hep-ph/0407333.
[55] P. Huber, J. Kopp, M. Lindner, M. Rolinec, and W. Winter, Comput. Phys. Commun. **177**, 432 (2007), hep-ph/0701187.
[56] M. C. Gonzalez-Garcia and M. Maltoni, Phys. Rept. **460**, 1 (2008), arXiv:0704.1800 [hep-ph].
[57] M. Maltoni and T. Schwetz, Phys. Rev. **D76**, 093005 (2007), arXiv:0705.0107 [hep-ph].
[58] E. Akhmedov and T. Schwetz, JHEP **1010**, 115 (2010), arXiv:1007.4171 [hep-ph].
[59] M. Maltoni and T. Schwetz, Phys. Rev. **D68**, 033020 (2003), arXiv:hep-ph/0304176.
[60] M. Gonzalez-Garcia, M. Maltoni, and J. Salvado, JHEP **1008**, 117 (2010), arXiv:1006.3795 [hep-ph].
[61] J. Hamann, S. Hannestad, G. G. Raffelt, I. Tamborra, and Y. Y. Wong, Phys.Rev.Lett. **105**, 181301 (2010), arXiv:1006.5276 [hep-ph].
[62] E. Giusarma, M. Corsi, M. Archidiacono, R. de Putter, A. Melchiorri, *et al.*, Phys.Rev. **D83**, 115023 (2011), arXiv:1102.4774 [astro-ph.CO].
[63] G. Mangano and P. D. Serpico, Phys.Lett. **B701**, 296 (2011), arXiv:1103.1261 [astro-ph.CO].
[64] J. Hamann, S. Hannestad, G. G. Raffelt, and Y. Y. Wong, JCAP **1109**, 034 (2011), arXiv:1108.4136 [astro-ph.CO].
[65] L. Bento and Z. Berezhiani, Phys.Rev. **D64**, 115015 (2001), arXiv:hep-ph/0108064 [hep-ph].
[66] A. Dolgov and F. Takahashi, Nucl.Phys. **B688**, 189 (2004), arXiv:hep-ph/0402066 [hep-ph].
[67] G. Karagiorgi, M. Shaevitz, and J. Conrad, (2012), arXiv:1202.1024 [hep-ph].
[68] D. G. Michael *et al.* (MINOS), Nucl. Instrum. Meth. **A596**, 190 (2008), arXiv:0805.3170 [physics.ins-det].
[69] G. Ambrosio *et al.* (VLHC Design Study Group), (2001).
[70] A. Y. Rodriguez Marrero, .
[71] Y. Kudenko (T2K), Nucl. Instrum. Meth. **A598**, 289 (2009), arXiv:0805.0411 [physics.ins-det].
[72] D. Greiner, T. Lachenmaier, J. Jochum, and A. Cabrera, Nucl. Instrum. Meth. **A581**, 139 (2007).
[73] Z. Sadygov, (1996), russian patent No. 2102820.
[74] N. Bacchetta *et al.*, Nucl. Instrum. Meth. **A383**, 263 (1996).
[75] V. Balagura *et al.*, Nucl. Instrum. Meth. **A564**, 590 (2006), arXiv:physics/0504194.
[76] M. Yokoyama *et al.*, Nucl. Instrum. Meth. **A622**, 567 (2010), arXiv:1007.2712 [physics.ins-det].
[77] N. Mokhov, J.Nucl.Sci.Tech. **S1**, 167 (2000).
[78] W. Winter, (2012), arXiv:1204.2671 [hep-ph].
[79] H. Minakata, H. Sugiyama, O. Yasuda, K. Inoue, and F. Suekane, Phys.Rev. **D68**, 033017 (2003), arXiv:hep-ph/0211111 [hep-ph].
[80] P. Huber, M. Lindner, T. Schwetz, and W. Winter, Nucl.Phys. **B665**, 487 (2003), arXiv:hep-ph/0303232 [hep-ph].
[81] C. Giunti, M. Laveder, and W. Winter, Phys.Rev. **D80**, 073005 (2009), arXiv:0907.5487 [hep-ph].
[82] J. Tang and W. Winter, Phys.Rev. **D80**, 053001 (2009), arXiv:0903.3039 [hep-ph].